

High Precision Nail-Penetration Setup for the Controlled Thermal Runaway Initiation of Lithium-Ion Cells at Very Low Temperatures

Nils Böttcher, Shahabeddin Dayani, Henning Markötter, Alexander Bau, Max Setzchen, Anita Schmidt, Julia Kowal, and Jonas Krug von Nidda*

A high precision nail-penetration (NP) tool for characterizing the mechanically induced thermal-runaway (TR) of lithium-ion battery (LIB) cells in a defined range of temperatures down to $-140\text{ }^{\circ}\text{C}$ was developed. To understand the cell specific behavior at low temperatures aiming at the determination of safe handling conditions, different scenarios are analyzed. First, accuracy tests of the NP-tool regarding motion and penetration depth are conducted with cylindrical cells at different temperatures. Thus, postmortem computer tomographic (CT) images are compared to the data measured with the newly integrated 3-axis force sensor which is further combined with a high-resolution position sensor. The herein developed setup allows evaluation of the NP-metrics at an accuracy of ± 1 pierced electrode layer without CT-scans. Further NP examinations at $20\text{ }^{\circ}\text{C}$ of fully charged cylindrical lithium nickel manganese cobalt oxide cells reveal a reproducible minimum damage as a reliable TR-trigger. Moreover, NP-tests at low temperature disclose a relation of the short circuit conductivity and TR-reactions during subsequent rethermalization to room temperature. Finally, the implementation of a novel fixture for a controlled very fast cooling of LIB-cells during critical damage opens the way to investigate the individual steps during a TR and, thus, to gain important information of the specific TR-mechanism of different LIB-cells.

1. Introduction


Electrical energy storage devices accelerate the transformation to a zero-carbon emission power supply. Among different types of storage devices, lithium-ion batteries (LIB) will remain one of the key technologies for the next decades. LIBs operating in their specified thermal, electrical, and mechanical range normally do not lead to safety issues. Exceptions remain from production defects like metal inclusions which can lead to unpredictable long term safety behavior.^[1] Nevertheless, critically damaging LIBs can result in catastrophic consequences due to a thermal runaway (TR). Additionally, the handling and transportation of damaged LIBs need special requirements. The conditions for the transport of critically defective LIBs are defined in the *Agreement concerning the International Carriage of Dangerous Goods by Road* (ADR) under special provision 376. However, current transport containers for critically damaged LIBs provide only a reduction of the TR effects. It is well known that applying very

low temperatures to LIBs reduces their reactivity.^[2–4] Furthermore, cooling with liquid nitrogen also enables the opportunity to stop the TR process itself or at least reduce the impact of the TR.^[5–8] Several safety tests regarding the transportation of LIBs defined in UN38.3 do not require a reproducible TR-trigger. Scientifically, the most discussed TR-triggers are heating, overcharging, external short circuit, and nail penetration (NP). The aimed investigation of the TR-behavior at low temperatures excludes heating as TR-trigger due to the external temperature input. Overcharging cells at low temperatures usually generates plating.^[9] However, the severity of lithium metal deposition on the anode depends on the exact temperature. Moreover, plating effects are partially reversible being especially favored at lower temperatures.^[10,11] As herein different (low) temperatures should be investigated, plating cannot be regarded as a repeatable TR-trigger. Furthermore, LIBs can show a voltage drop down to 0 V at very low temperatures, e.g., upon submersion in liquid nitrogen. This effect can be connected to a very large internal resistance, most probably, caused by the strongly reduced ionic conductivity.^[12] Thus, already very low currents would lead to a severe voltage

N. Böttcher, S. Dayani, H. Markötter, A. Bau, M. Setzchen, A. Schmidt, J. Krug von Nidda

3.1 Safety of Dangerous Goods Packaging and Batteries
Bundesanstalt für Materialforschung und -prüfung (BAM)
Unter den Eichen 87, 12205 Berlin, Germany
E-mail: jonas.krug-von-nidda@bam.de

N. Böttcher, J. Kowal
Institut für Energie- und Automatisierungstechnik
Technische Universität Berlin
Einsteinufer 11, 10587 Berlin, Germany

 The ORCID identification number(s) for the author(s) of this article can be found under <https://doi.org/10.1002/ente.202301379>.

© 2024 The Authors. Energy Technology published by Wiley-VCH GmbH. This is an open access article under the terms of the Creative Commons Attribution License, which permits use, distribution and reproduction in any medium, provided the original work is properly cited.

DOI: 10.1002/ente.202301379

response without significantly changing the cell's state of charge. Nevertheless, plated lithium was identified as possible TR-trigger induced by fast charging at temperatures above 20 °C.^[13]

The external short circuit (SC) setup has already been used successfully by Grandjean et al. for low temperature investigations on Panasonic 18 650 cylindrical cells.^[3] A minimum SC-temperature of −35 °C could be defined to prevent a TR. Nevertheless, the surface temperature of the cells tested raised to a maximum of −11 °C. The raising cell surface temperature—although a TR reaction was prevented—contradicts a full inertization of the internal cell reactions.

The most controversial abuse test for LIB safety investigation remains the NP. Nonetheless, the widespread use of NP supports its general suitability for abuse testing.^[14–21] Furthermore, an NP typically causes severe damage to a LIB and, thus, clearly results in critically damaged cells. Among multiple parameters, the nail diameter, penetration speed, penetration depth, and the penetration position can have a great influence on the intensity of the occurring TR.^[22] Another interesting factor is the possibility to couple a NP set-up with further high-precision sensing, especially, regarding the observation of the penetration of individual layers. Intriguingly, it is possible to follow the course of the NP by direct observation with a high-speed X-ray inspection system, as shown by Yokoshima et al. during the step-wise penetration of LIB pouch cells.^[23,24] The high-speed imaging coupled with the recorded multiple voltage drops indicated the layer-by-layer internal short-circuit formation. Similar effects could be observed with the respective high-precision tool developed by Huang et al. and by Qi et al. based on the sensing of multiple in-situ temperature peaks at the nail tip prior the TR and changes in the voltage signal at millivolt level, respectively.^[25,26]

At ambient temperatures, it was shown that the electric conductivity of the nail has no significant influence on the general TR-behavior during an NP test.^[13,19] Anyway, it should be mentioned that during a NP at low temperatures the cell temperature is increased locally due to the temperature of the nail itself independent of abuse-based processes. A very recently published paper by Sunderlin et al. investigated the NP of commercial 5 Ah lithium battery cells under liquid nitrogen submersion.^[27] The cells comprised LiNi_{0.8}Mn_{0.1}Co_{0.1}O₂ (NMC 811) as cathode active material. The results reveal a self-heating of the cells at −60 °C. Furthermore, all penetrated cells went into TR during rethermalization to ambient temperature.

Moreover, the submersion to liquid nitrogen without abuse causes no damage to LIB-cells according to various publications.^[28,29] Nevertheless, Leonhardt et al. discovered that (liquid) nitrogen can leak into the cell during the submersion process depending on the process duration.^[30] Thus, the current interrupt device was triggered in some cylindrical cells. Furthermore, some pouch cells showed a swelling after the rethermalization to room temperature.

However, determining the specifications needed for cooled, thus, safe transport conditions require a detailed understanding of the reactions occurring at low temperatures. Moreover, resulting hazards upon rethermalization of the cooled cells to ambient temperatures need to be investigated. Furthermore, new cell developments, especially, for low temperature applications require a reliable and reproducible setup to define cell-specific conditions for a cooled transport.

Additionally, the inertization mechanism itself is not fully understood yet. The reduced ionic conductivity of the frozen electrolyte was suggested as one of the main reasons for the mitigated reactivity of LIB-cells at low temperatures.^[12,27,31] The generally limited electrical energy release of cells at low temperatures could also reduce the TR-probability during rethermalization of damaged cells to ambient conditions. Finally, understanding these relations can ensure that the transport temperature chosen is sufficiently low to assure the safety of the specific cell/battery to be transported. Additionally, the utilization of a transport temperature only as low as needed ultimately leads to a reduced energy consumption during a cooled transport.

While a recovering voltage after rethermalization from a NP-abuse was already shown by Grandjean et al. a full inertization at very low temperatures combined with a defined NP-abuse could also enable the formation of critically damaged cells that are still in operating conditions upon rethermalization.^[4] Thus, the in-depth investigation of critically damaged cells, e.g., with electrochemical impedance spectroscopy (EIS) or X-ray computed tomography (XCT), could be realized.

The present work targets the development of a highly precise NP abuse setup which is capable of investigating LIB cell damage behavior down to −140 °C with a spatial resolution of 10 μm enabling the penetration of single electrode layers. Hence, a mechanically reproducible NP test (NPT) can be realized at low temperatures allowing the accomplishment of the two main goals aforementioned: 1) the determination of the cooled transport conditions, and 2) the enabling of in-depth exploration of inertization and TR mechanisms of commercial LIB cells.

A fast and variable sampling measurement system up to 10 kHz was combined with a 3-axis force sensor, high-resolution position sensing and a cold gas system, to achieve the desired precision in this NP abuse setup. Various experiments were carried out with this newly developed abuse setup, beginning with the validation of its mechanical capabilities employing completely discharged LIB-cells. The results were evaluated based on the force sensor data and postmortem CT analysis. Moreover, conducting NPTs on fully charged cells at room temperature facilitated the investigation of NP-driven internal short circuit reactions in a new fashion. Allowing a rather precise definition of the penetration depth needed for reliably triggering the TR in a specific cylindrical lithium nickel manganese cobalt oxide (NMC) cell. Furthermore, the set-up was used to show the possibility to study the effects when a cell is damaged at very low temperature and rethermalized to ambient temperature. Additionally, the set-up was extended by a movable liquid nitrogen bath below the cell holder enabling shock-cooling during abuse tests. Finally, the set-up was utilized to demonstrate the differences of NP abuse investigations at low temperatures compared to ambient conditions.

2. Results and Discussion

2.1. Design of the High-Precision NP Tool

Abuse testing of LIBs requires a gas-tight and flame-proof environment. **Figure 1a** shows the 246 L stainless steel test chamber including the herein newly developed abuse setup. With a

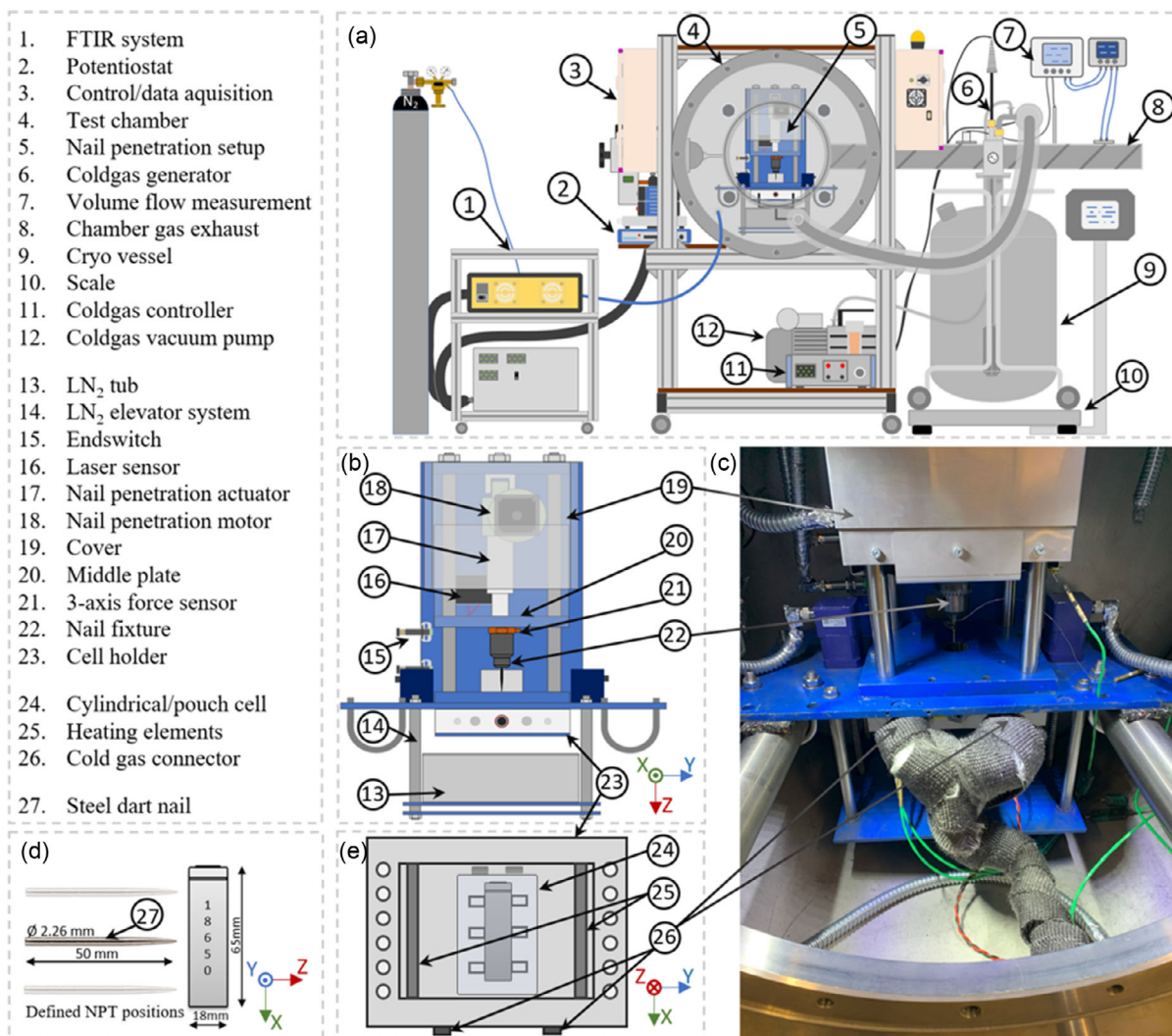


Figure 1. a) Overview of the test bench with all components. b) Schematic representation of self-developed NP setup with shock cooling option mounted. c) Photograph of the set-up with mounted cold gas option. d) Three possible penetration positions with example cell. e) Universal thermally insulated cell holder including heating elements.

maximum validated working pressure up to 6 bar, this chamber can handle test conditions resulting in excess pressure. In the current work, the chamber is typically operated under nitrogen flow or in the presence of LN_2 . To generally avoid overpressure from the nitrogen flow, all tests were performed under ambient pressure realized by an open exhaust system connected at the back. The gas flow of the nitrogen as well as the gas volume emitted during a TR can be measured by a volumetric pressure differential sensor and a temperature difference sensor in the exhaust pipe. The system can be coupled with a Fourier-transform infrared (FTIR) spectroscope to conduct a compositional analysis of the emitted gases. The corresponding FTIR-probe is located at the connection between the chamber and the exhaust pipe.

The FTIR-exhaust is connected to the front of the test chamber. Hence, the FTIR gas flow works in a closed loop. Such an operating condition is beneficial as the gas concentration in the chamber is not changed by the FTIR measurements itself over

time. A real time control is required during an NPT to follow the very fast processes. This is realized with a LabVIEW based CRIO system. Moreover, this system allows to easily acquire data from different sources in multiple sampling rates. Detailed overview of the newly developed NP tool is shown in Figure 1b. A linear actuator equipped with a 24 V DC motor or a NEMA 23 stepper motor was used to fit the speed requirement defined in the standard SAE j2464 (80 mm s^{-1}) as well as the one defined in the ECE Trans 100 ($1\text{--}10 \text{ mm s}^{-1}$). However, the minimum moving distance of 0.08 mm is only achieved by the stepper motor (1.6 mm s^{-1} with 200 steps s^{-1}). The DC motor as well as the stepper motor are equipped with rotary encoders to measure the motor position. Furthermore, the 0.01 mm high-resolution motion measurement of the nail is achieved by using a laser triangulation sensor. This sensor directly measures the movement of the middle plate (see Figure 1b). The middle plate is machined from 2 cm thick steel and links the nail fixture with the linear actuator. Four linear guides ensure a tilt free motion of the

middle plate. A drill chuck connects the 3-axis piezo force sensor, the middle plate, and the linear actuator. Thus, the force-sensor mainly measures the spatial behavior of the nail. A drill chuck as nail fixture has proven suitable for NP tools as it is very convenient to switch in between different nails. In the developed set-up, a large variety of penetration tips with numerous shapes can be used up to a diameter of 13 mm. Two inductive sensors located at the end positions prevent the linear actuator from moving to its mechanical limits, hence, preventing its damage.

The rather challenging combination of defined thermalization of LIB-cells at very low temperatures with abuse testing was realized herein by the use of a nitrogen cold gas generator system. The cold gas generator system works with two heating elements, a jet element and a heater element installed in the cryogenic vessel and the output hose, respectively. The former regulates the gas flow and the latter the gas temperature. This way the cold gas system can generally provide a continuous and temperature-controlled nitrogen gas flow from 100 to $-190\text{ }^{\circ}\text{C}$. The vacuum isolated hose directs the nitrogen gas flow into the chamber (Figure 1c). At this location, the gas flow is redirected with 10 mm PTFE tubes to the thermally isolated cell holder. Before entering the cell holder, the gas flow is divided, which ensures a homogenous cooling of the cell. The cell holder, fabricated from flame-proof calcium silicate (AGK CS1002si), thermally insulates the LIB-cell (Figure 1e). To realize different penetration positions with a high degree of repeatability, the cell holder is equipped with a fixed hole pattern (see Figure 1d). Furthermore, this cell holder design easily allows the test of different cell formats as indicated in Figure 1e.

FTIR- as well as EIS-measurements and tests at elevated temperatures are not in the scope of the present manuscript. For completeness, these features are exemplarily discussed for few cells. Moreover, the lower temperature range which can be achieved in a controlled manner for the device under test depends mainly on the thermal isolation of the cell holder. The range was exemplarily checked with an 18 650 cell. First, the cell was cooled down with a N_2 -flow set to $-190\text{ }^{\circ}\text{C}$, reaching a constant temperature of $-140\text{ }^{\circ}\text{C}$ (see Figure S1, Supporting Information). After rethermalization, the same cell was set at a controlled temperature of $20\text{ }^{\circ}\text{C}$, as shown in Figure S2, Supporting Information. At this stage, an EIS-measurement was performed revealing the typical Nyquist plot of an LIB-cell (see Figure S2b, Supporting Information). The cell was further heated with the N_2 -flow reaching a stable cell temperature of $70\text{ }^{\circ}\text{C}$. Furthermore, a NPT was performed at this temperature leading to the typical voltage and temperature trend of a TR (see Figure S2a, Supporting Information). In order to demonstrate the ability to conduct gas analysis with the designed NP test stand, four NPTs were conducted at room temperature, where the composition of the gas was evaluated with the connected FTIR which was operated in a closed loop (see Figure 1a). Details of the respective NPTs are stated in Table S1, Supporting Information. Exemplarily, the time-resolved concentration of four typical species for LIB vent gases, i.e., carbon monoxide (CO), dimethyl carbonate (DMC), ethylene carbonate (EC), and hydrogen fluoride (HF), are shown in Figure S3, Supporting Information. After the typically observed overshoot during the initial moments of the measurement, a rather stable concentration of the different gases can be detected (see grey area of Figure

S3, Supporting Information). This region can be used to calculate the concentration of a certain gas species in the homogenized gas mixture after the TR. Generally, the FTIR data reveals that the measurements are rather reproducible down to a low ppm concentration. Especially the EC-measurements shows however that repeatability measurements are needed to gain trustable statements.

Finally, the NP setup was extended with a shock cooling device which can be operated independent of the NP tool. To guarantee a stable cell temperature, even when the tub below the cell holder is filled with liquid nitrogen, the aforementioned cell holder was additionally equipped with two heating elements (300 W each). Decoupling the NP test from the shock cooling device enables the opportunity to rethermalize the cell after the test with and without leaving the nail in the cell. Thus, a non-conductive nail test can be simulated by penetrating the cell with a conductive nail at very low temperatures and withdrawing it prior rethermalization.

2.2. Motion Accuracy of the NP Tool

To provide the highest possible accuracy of the NP depth, the motion control of the stepper actuator was first validated for three different control modes without penetrating a battery cell. The open loop control processes the number of required steps to move to a certain position without measuring the actual position. This control mode is common for stepper motors.^[32] In the closed loop mode, an encoder on the stepper shaft returns the motor position, which allows to correct the required motor steps by the real motor steps done. Thus, the closed loop mode allows the correction of missing steps. In the present work, another closed loop mode was tested as a third option by using a laser sensor (LS) signal as feedback to calculate the necessary steps during the movement instead of the encoder on the stepper. For accuracy analysis, the LS-sensor signal was analyzed for all control modes between 0.5 and 40.5 mm mimicking the needed distance for a NP-test of the herein investigated LIB-cells. For each control mode, the NP-tool movement was investigated at different combinations of speed and distance. This generates a test plan with a total number of 15 tests, i.e., five tests per control mode. During each test the tool was moved the respective distance, resulting in different total number of motion steps. During this process the deviation of each individual motion step was recorded. It must be considered that this test procedure leads to an unequal number of data points according to the different numbers of motion steps for each test. Thus, for better comparability of the tests, the occurring deviations between each motion step was analyzed. The average motion deviation of the desired set point is depicted as markers in **Figure 2**. The corresponding whiskers show the respective maximum and minimum motion deviation from the setpoint of each test. The detailed information of all test results are provided in Table S2, Supporting Information.

Generally, the absolute deviation from all performed motion steps is rather small over all tests. The highest deviations per step were measured during the test with the closed loop encoder mode at a speed of 1 mm s^{-1} and a 5 mm motion step, showing a minimum and maximum value of -0.07 and 0.065 mm ,

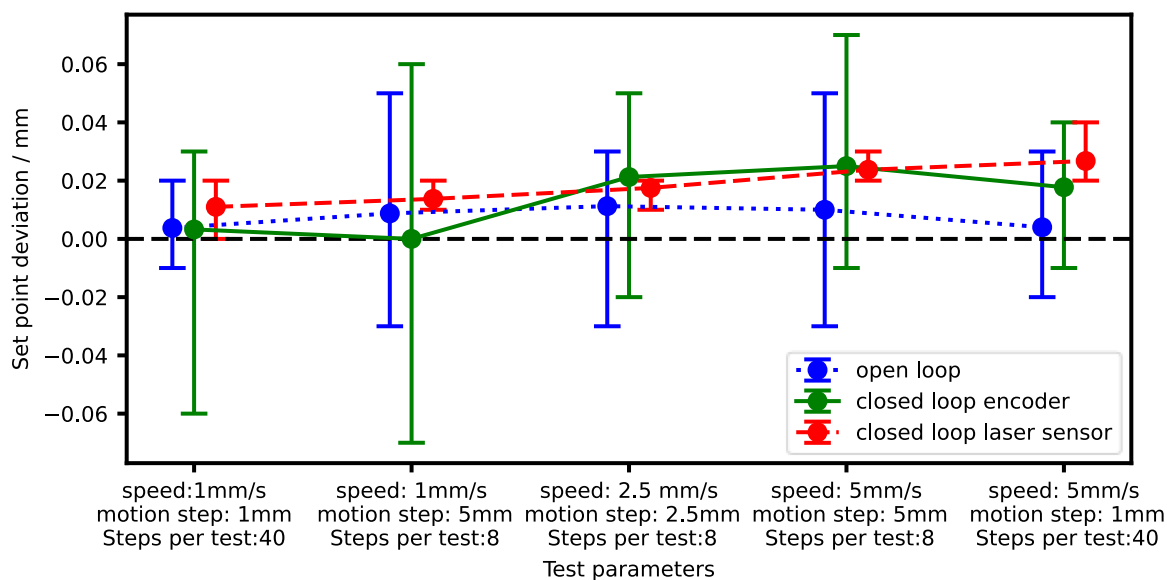


Figure 2. Deviation of motion accuracy tests with the three control modes and different test conditions. Markers represent the mean deviation of the occurring deviation between each motion step. The whiskers represent the respective maximum and minimum motion deviation from the setpoint of each test.

respectively. Evaluation of mean deviations of the open loop control mode hints to a relatively speed independent behaviour, as an increase in motion speed does not result in an increase in average deviation. Interestingly, the closed loop control mode shows a combined trend of speed and motion dependency on the mean deviation if the test with the highest absolute deviation is disregarded. This is indicated by the nonlinear rising of the mean deviation with increasing speed. Analysis of closed loop LS control mode reveals that in this case higher motion speeds as well as larger motion steps continuously lead to a higher average deviation. This points toward the fact that the implemented control algorithm does not compensate the mass inertia and explains the tendency to slightly overshoot the desired motion setpoint during all tests. However, the absolute deviation region at each test is clearly the smallest for the LS closed loop mode, independent of speed and step width. Since the mean offset at the LS closed loop mode was always greater than 0.01 mm, exceeding the minimum increment of the stepper, it is possible to include a respective general offset correction. This reduces the overall error without significantly undercutting the desired setpoint. Furthermore, due to its direct link with the nail fixture, the LS-based closed loop control guarantees a motion control independent from possible attritions of the actuator. Detailed information of test results is provided in Table S2, Supporting Information.

2.3. NPTs at Ambient Temperature

To investigate mechanical reproducibility, recorded data of full NP tests were analyzed in detail and further supported with X-ray computed tomography (CT). Rotational symmetric 18 650 cells were used since they are well-known to be suitable for CT-imaging, also during TR.^[33–36] The herein investigated

lithium iron phosphate (LFP) cells were fully discharged to minimize occurring TR-reactions, hence, avoiding TR-induced reproducibility issues. Furthermore, this procedure enables evaluation of the mechanical quality of the nail test by postmortem CT as the final damage pattern stays intact after the NPT. The measurement in **Figure 3a** shows the force data progress of two fully penetrated LFP cells (LFP-1 and LFP-2). Detailed parameters of the LFP-cells can be found in Table 2. **Figure 3b** depicts a respective postmortem CT-slice showing the center of the NP pathway. As a result of the round geometrical construction of cylindrical cells, the mechanical progress of the nail generally tends to deviate during testing. Typically, the electrode layers of cylindrical cells are wrapped around a metal rod which also needs to be penetrated if a complete penetration of a cell is targeted.

The z-force of the 3-axis force sensor shown in **Figure 3a** represents the force in the direction of the nail motion. Furthermore, the y-force and x-force provide information about the nail's lateral movement. After reaching the metal rod in the cell center, approximately at 8 mm, the y-force of cell LFP-1 starts to increase to -50 N indicating a lateral movement during the nail test. This is also confirmed by the measured lateral error in the postmortem CT of LFP-1 in **Figure 3b**. Interestingly, the slightly smaller increase in y-force of LFP-2 (i.e., -20 N) at the same point can be connected to a less severe lateral error according to the postmortem CT.

On the one side, this demonstrates the reasonable usability of a 3-axis force sensor to identify the quality of the NP itself. On the other side, it seems like the mechanical reproducibility of a NP test of cylindrical cells could be improved by simply not penetrating the full cell. However, this requires detailed knowledge about minimum number of penetrated layers/minimum depth needed for reliably triggering a TR. Generally, the ability of a NP to trigger a TR can be related to the released amount of stored energy over a certain time range.

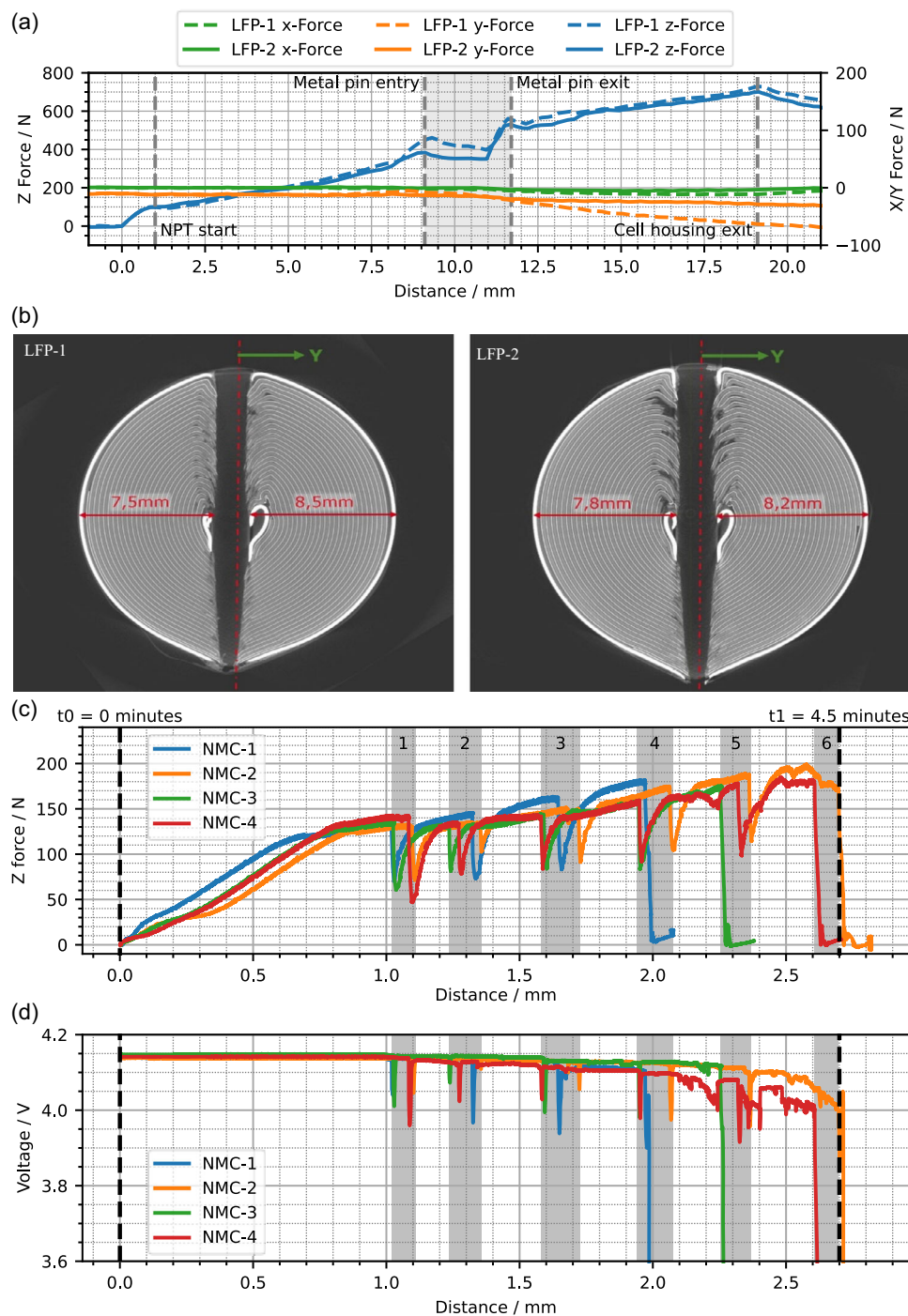


Figure 3. Investigation of the mechanical reproducibility during the NPT (at 45 mm s^{-1}) of fully discharged 18 650 LFP-cells, showing a) the force sensor data and b) the respective postmortem CT images of LFP-1 and LFP-2. Exploration of the minimum penetration depth required for a reliable TR during a NPT (at 0.01 mm s^{-1}) utilizing fully charged NMC-cells, showing c) the z-force and d) the voltage trend of NMC1–4 with marked short circuits. The details of the NPTs can be found in Table S1, Supporting Information.

Aiming toward a rather reactive cell chemistry, the following tests were performed at 20°C with four cells of the herein investigated NMC cell type at a state of charge (SOC) of 100% (NMC-1 to NMC-4). Detailed parameters of the NMC cells are summarized in Table 2. Figure 3c depicts trend of cell voltage, z-force,

and cell temperature in respect to test time during the very first moments of an NPT performed with a speed of 0.01 mm s^{-1} . This very slow penetration speed was chosen on purpose for the determination of the minimum penetration depth, as at slower speeds less severe mechanical damage is created by

the nail.^[21] Since the voltage drop below 3.8 V was directly followed by a TR, the voltage progress was cut off to better visualize the short circuit behavior. The z-force trend and the corresponding voltage trend with the full range down to 0 V are shown in Figure S4a and S4b, Supporting Information, respectively. Prior to the NPT, the nail was moved manually toward the cell housing. After the beginning of the NPT, the first raise in the z-force shows the deformation of the cell housing. Interestingly, multiple quick, short drops in the z-force were observed during the further experiment which can be related to the stepwise penetration of individual cathode current collectors. Each of those drops in z-force is typically coupled with a rather small and short drop in cell voltage. Hence, it can be assumed that the first three to six internal short-circuits induced by NPT were rather mild not really leading to a strong TR. These so-called soft short circuits seem to disappear immediately after releasing a small amount of energy as indicated by the almost full recovery of the initial cell voltage. The occurrence of soft short circuits—even though a conductive nail was used—hints to a strong dependency of the utilized nail geometry and nail speed on the abuse effect. Similar effects were also investigated by Lamb et. al.^[16]

However, the voltage dropped very quickly to 0 V at the 4th, the 5th, or the 6th internal short-circuit for different tests. Such a voltage drop indicates a hard short circuit, which abruptly releases a vast amount of the stored energy. This was accompanied by a very quick increase in temperature instantly leading to a TR. According to this observation, that a single hard short circuit seems to release enough energy to start the TR reaction, it should be possible to instantly trigger a TR by only a single layer short circuit if a suitable NPT configuration, including the nail is utilized.

To allow a statement on the minimum penetration depth needed for a TR, the according test series consisted of four repetitions. Employing the herein defined nail test configuration, the TR appeared after four to seven penetrated layers for the herein tested NMC-cell. Thus, a minimum NP depth of 3 mm can be defined as a reproducible TR trigger for this cell type.

2.4. Validation of the Penetration Depth

In the following section, the NPT of the utilized NMC cell type is discussed depending on the pre-treatment temperature. Either, the cells were pre-treated and abused at ambient temperature (20 °C), or they were submersed in LN₂ prior to abuse. The latter represents the lowest temperature boundary condition of the present work. Performing equivalent NPTs with 5 mm depth at a speed of 5 mm s⁻¹ guarantees to achieve the minimum penetration depth discussed in the prior Section 2.3.

Figure 4a,b show the CT of a fully discharged NMC cell penetrated at 20 °C (NMC-5, discharge cut-off voltage 2.5 V). Investigating the worst case regarding the precision of the penetration depth, by losing motion steps during the penetration process, this NPT was performed in the open loop control mode. The CT analysis in Figure 4a reveals twelve fully penetrated layers with a maximum measured penetration depth of 4.95 mm. The maximum depth was calculated from the red circle fitted around the cells housing to the deepest entry of the nail tip.

This circle also indicates that the cell penetrated at low temperatures shows a slight deformation appearing at the housing.

Since the measured motion data in Figure 4e indicates a 5 mm depth, a deviation of 0.05 mm remains. As the CT was performed after the nail was removed from the cell, the difference could occur due to the elasticity of the not-penetrated layers, i.e., the remaining layers between the deepest penetration point and the metallic rod. Those layers are not-penetrated, however, are clearly deformed. The mentioned elasticity effect is also supported by the reduced airgap between the not-penetrated layers and the metal rod on the nail entry side (see Figure 4b). Additionally, this effect could also be caused by the measurement procedure. It starts measuring from outside at one of the two sides. Before the NPT the outer side was curved, hence 50 μm could just be lost due to the lost part of the curvature. This also explains the observable gap between the metal rod and the not-penetrated layers, although the metal rod was almost fully pushed to the electrode layers on the opposite side (Figure 4d). The measured gap difference of 0.220 mm can explain most of the 0.33 mm missing in penetration depth. Nonetheless, the achieved depth clearly exceeds the requirement of a minimum penetration depth of 3 mm. Furthermore, the quite similar trend in x- and y-force for both tests show the general mechanical reliability of the herein developed NPT. To ensure comprehensiveness, Figure S5, Supporting Information, illustrates the respective voltage trends for both tests. The mechanical reliability is further confirmed by a noticeable angle of ≈90° between the nail imprint and the metal rod in Figure 4b, d, which can be related to the x-force data in Figure 4f. This applies equally to Figure 4a,c in connection to the y-force in Figure 4f. Comparing the CTs of the NPT at 20 °C and of the cell submersed in LN₂ in detail reveals further differences in the damage pattern. In both cases electrode layers are bent in the regions close to the nail. However, only the CT-image of the LN₂ submersed cell further reveals compressions in the copper current collector (region highlighted in orange in Figure 4a, c). This effect can be directly related to the frozen state of the cell and the comparatively high amount of required force for the NPT. Furthermore, this probably is also the reason for the more pronounced layer bending close to the metal rod in the cell center observed for the same cell (Figure 4a,c pink circles). Analyzing the layer edge at and the shape of the penetrated region itself, both cells reveal a different damage pattern. While the CT-image of the cell damaged at 20 °C (Figure 4a,b) shows a more roundly penetration shape, the penetration shape of the frozen cell (Figure 4b,c) tends to be straight. This observation can be linked to the difference in the occurring reactions during the NPT. An NPT at room temperature directly leads to reactions in the short-circuited layers, hence, resulting in missing active material. This effect is also indicated by the rough edges of the short-circuited layers. Contrarily, no direct reactions occur inside the cell penetrated in a frozen state.

2.5. NPT at Low Temperature

Determining the conditions for a cooled, safe transport for LIBs requires standardized test methods employing investigations at defined thermal conditions. For these tests the cold gas generator

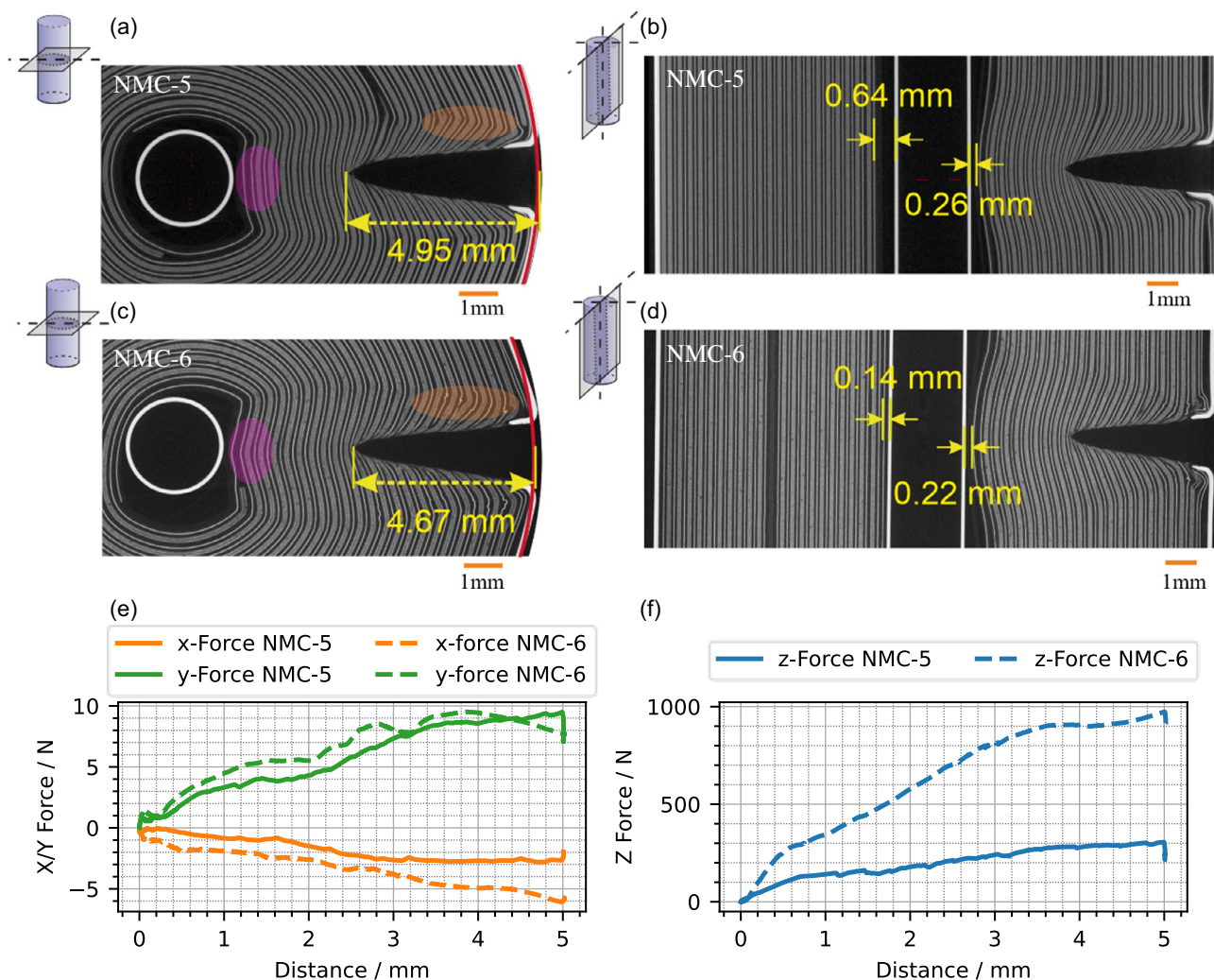


Figure 4. a,b) Postmortem CT of the discharged NMC-5 cell at 20 °C after NPT. c,d) postmortem CT of discharged, LN₂ submersed NMC-6 cell after thawing to room temperature. e) Z-Force Data of NMC-5 and NMC-6. f) XY-Force Data of NMC-5 and NMC-6. The corresponding voltage trend of NMC-5 and NMC-6 can be found in Figure S5, Supporting Information.

introduced in Section 2.1 provides the continuous and constantly tempered flow of nitrogen realizing the desired NPT temperatures. **Figure 5** exemplarily depicts the temperature (Figure 5a) and the voltage trend (Figure 5b) during the NPT of two different, fully charged cylindrical NMC cells at $-85\text{ }^{\circ}\text{C}$ ($\pm 5\text{ }^{\circ}\text{C}$) including the rethermalization to room temperature. The temperature and voltage behavior overview of the corresponding four test repetitions can be found in Figure S6, Supporting Information. All tested cells were passively heated by convection after stopping the cold gas flow and, thus, rather slowly rethermalized to ambient temperature. Generally, a self-heating of the cells can occur due to internal reactions induced by the NPT-damage. While four cells were rethermalized with the nail remaining in the cell (NMC-11 to NMC-14), the other four samples were thawed after removing the nail (NMC-7 to NMC10). For the second purpose, the nail removal was conducted during the low temperature phase. Hence, reactions occurred only from the short circuits between the damaged electrode layers mimicking an NPT with a non-conducting nail.

The cells with a remaining nail typically showed a TR upon rethermalization reaching temperatures over 800 °C. More precisely, these cells first showed a small increase in voltage in the self-heating phase followed by an immediately drop in voltage to 0 V and a subsequent high increase in temperature. Apparently, the nail serves as electric conductor leading to a high amount of released electrical energy during thawing. Contrarily, cells with a removed nail showed only a slight increase in temperature up to 133 °C during rethermalization. Moreover, the voltage level from three of four cells immediately rose and stabilized after a rather low increase in temperature (see Figure S6, Supporting Information). It must be mentioned that the NPT parameters differed slightly between the two sets. For the set, where the nail was removed before rethermalization, a speed of $\approx 45\text{ mm s}^{-1}$ and a final NPT depth of $\approx 12\text{ mm}$ were used. Contrarily, the NPTs with the nail kept inside the cell during rethermalization were conducted with a speed of $\approx 5\text{ mm s}^{-1}$ and a final NPT depth of $\approx 6\text{ mm}$. Considering the respective NPT criteria, the first set of parameters can be regarded as

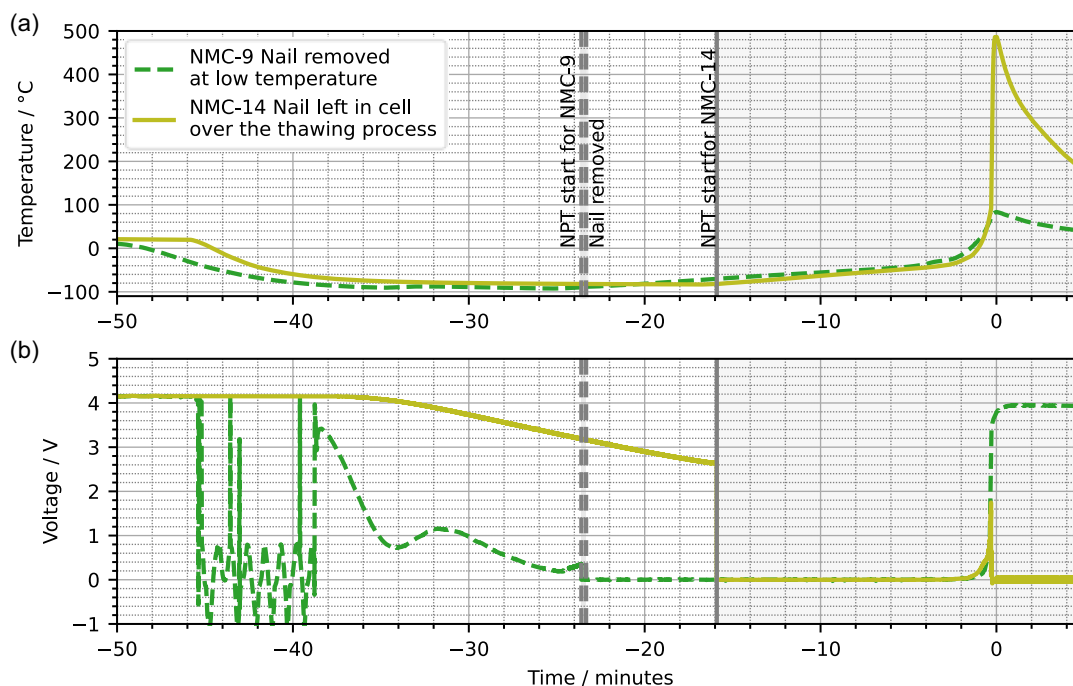


Figure 5. a) Cell temperature and b) corresponding cell voltage during NPT after precooling with and without nail remaining inside the cell during rethermalization to room temperature. (The time was synchronized at the occurrence of the maximum temperature).

the ones possibly inducing a more severe mechanical damage. Interestingly, these tests nonetheless showed clearly less severe behavior during rethermalization, indicating a minor influence of the NPT parameters themselves compared to the conductivity of the nail regarding TR-harshness during rethermalization. Overall, the results reveal that removing the nail at low temperatures and subsequent thawing can lead to so-called critically damaged cells.

Generally, critically damaged cells can be understood as damaged/abused cells in an uncertain safety state. The herein discussed cells were clearly damaged, however, still functional after the NPT only showing a slight self-discharge. In summary, the herein presented test method offers a rather unique, however, still reliable approach to produce critically damaged cells in working conditions. For the sake of completeness, it must be mentioned that the voltage measurement of the cell without the nail equipped in Figure 5 had a loose contact while cooling down as indicated by the voltage ripple. During the NPT, the voltage signal, nevertheless, was again readable. Presumably, the voltage reading issue was caused by uneven material shrinkage up on cooling leading to a poor contact of the bolted cell contact. To prevent this issue, all cells after this test series were contacted by spot-welding.

In summary, the tests are divided in two series: i) tests where the nail was removed before rethermalization and ii) tests where the nail remained in the cells during rethermalization. Although for test series i) compared to test series ii) the NPT was conducted with higher speed ($\approx 45 \text{ mm s}^{-1}$ vs. 5 mm s^{-1}) and with a larger depth ($\approx 12 \text{ mm}$ vs. $\approx 5 \text{ mm}$), no cell of test series i) showed a clear TR during rethermalization. However, the deeper penetration depth with a higher speed should induce a

larger cell damage. This reveals that the occurrence or non-occurrence of a TR during rethermalization is mainly influenced by the conductivity of the nail in the test conditions given.

2.6. Shock Cooling Tests

Investigating different states of the TR by freezing cells during abuse tests enables deep insights in the TR-mechanisms. **Figure 6a** shows the schematic illustration of the expected freezing process of a cylindrical cell upon submersion in liquid nitrogen. Assuming the cell freezes from the surface to the core, local TR-reactions should be rather situated at inner layers. Moreover, the process should allow the in-depth investigations of the TR-damage patterns with postmortem techniques. Adjusting the main parameters like the amount of liquid nitrogen (2.7–3 kg) and precooling time (0–20 s), nail depth (5 mm) enabled the repeatable freezing of the investigated NMC cell type. Initial tests, employing a shock cooling directly after starting the NPT (precooling time = 0 s) with a penetration depth of 5 mm remained unsuccessful for this cell type, as they always lead to a TR of the whole cell. Introduction of a short precooling time (6 s with 3 kg of LN_2), realized by rising the LN_2 -tub prior the NPT, allowed the aimed freezing of a TR-process. Additionally, it must be mentioned that fluctuations in the LN_2 -level largely influence the shock cooling time necessary. The voltage and z-force trend of two successful NPT-shock cooling experiments with NMC-cells are shown in Figure 6b. Apparently, the internal reactions of the cells seem to slow down after 3 mm penetration depth as indicated by a reduced drop in voltage and a continuous rise in z-force upon this point.

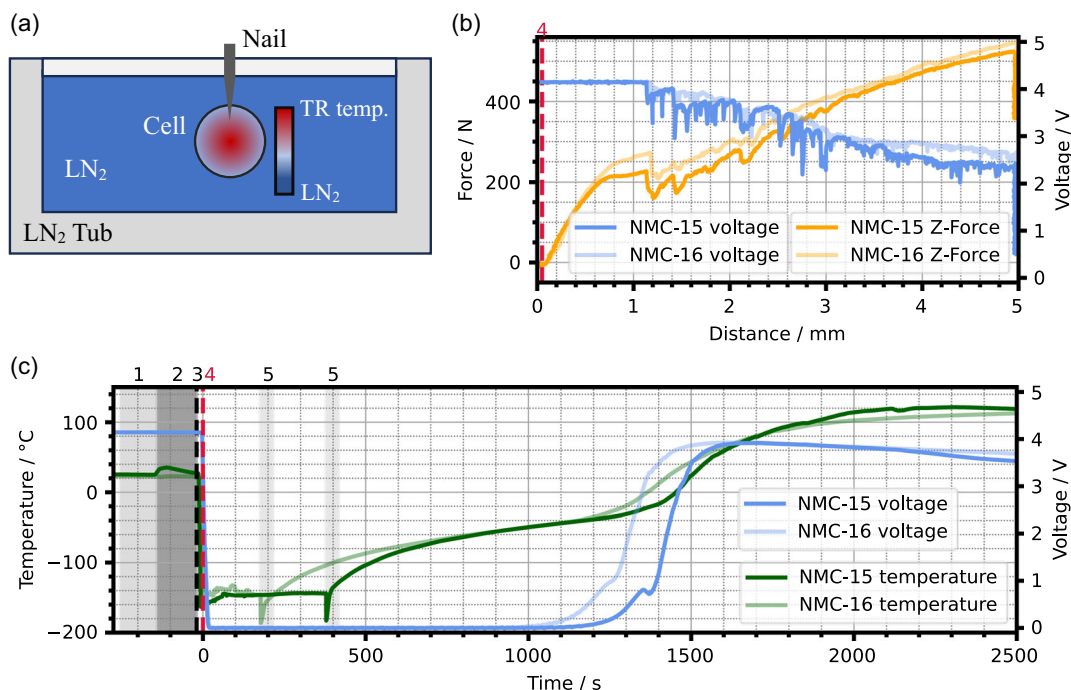


Figure 6. a) Schematic of expected cell temperature gradient during LN₂ shock cooling and NPT. b) Z-Force and voltage behaviour during NPT shock cooling experiments of NMC-15 and NMC-16. c) Corresponding temperature and voltage progress before, during and after shock cooling test, including the following steps: 1) Filling LN₂, 2) Temperature stabilisation with heating elements, 3) Start of shock cooling, 4) Start of NPT, 5) End of submersion and start of rethermalization.

Figure 6c visualizes the whole shock cooling test combined with an NPT. The shock cooling test is separated in five steps: 1) Liquid nitrogen is filled in the tub. To achieve a stable cell temperature during the filling process, the additionally installed heating elements are active during this time (see also Section 2.1). 2) The heating elements ensure the homogenization of the cell temperature to 22 ± 1 °C after the filling process. Due to the slight sprinkling of liquid nitrogen during filling, the possibility occurs that the surface temperature shortly increases after stopping the filling process. 3) Start of the tub movement and begin of the shock cooling process. 4) NPT with desired parameters, here 5 mm depth and 5 mm s^{-1} . For both tests, the nail was moved out of the cell again prior to step five. 5) Step five contains the tub movement back to its lower, thus, initial starting position, and the start of the rethermalization. Due to different initiation times of step five, the rethermalization started at different points in time during the herein presented tests.

Comparing the voltage readings just prior to the start of the NP of the shock cooling tests and of the tests with the rather long pre-cooling time (precooling-test) discussed in Section 2.5 reveals values of 4.2 and $2.0 \text{ V} \pm 1 \text{ V}$, respectively (see Figure 6b vs. Figure 5). The later value indicates that the cell was already inerted, caused by the longer cooling phase during that test. Contrarily, the measured cell voltage of 4.2 V for the shock cooling test does not hint to any inertization of the cell before the start of the NP. Generally, the shock cooling method also led to critically defective, however, still functioning cells. However, the shock cooling test resulted in slightly higher maximum temperatures during rethermalization as well as to a faster

decrease in cell voltage at the end of the test. Hence, the shock cooling test seems to generate more severe damages compared to precooling test. However, the TR seems to be locally restricted in both cases, indicating an incomplete cell internal propagation.

3. Conclusions

The combination of a NP setup with a 3-axis force sensor, high-resolution position sensing, a cold gas system and a fast-sampling measurement system up to 10 kHz allowed the desired development of a highly precise NP abuse test stand. This setup enables a wide range of new investigations related to the TR behaviour of LIBs, also at defined low temperatures. More precisely, NPTs at defined temperature values ranging from -140 to 70 °C are possible with an accuracy of ± 1 penetrated layers. Thus, the aimed determination of cell-specific cooled transport conditions can be conducted for a large variety of cell types. The investigations regarding the general accuracy of the setup lead to a new perspective on the standards for NPTs, allowing the definition of a minimum damage needed for reproducibly triggering a TR as exemplarily shown for cylindrical NMC-cells. Furthermore, the implemented 3-axis force sensor system combined with the high sampling rate revealed insights in the mechanical NPT progress, e.g., allowing the evaluation of the NPT quality without the need of further CT scans. Interestingly, the conducted experiments allowed the definition of a reliable method to create critically damaged, but still functioning LIB-cells. In these cells, the TR seems to be locally

confined pointing toward an incomplete cell internal propagation. The behaviour of these rather unique cells will be studied further in future investigations.

The range of possible experiments was extended by the implementation of a movable liquid nitrogen bath below the cell holder adding a shock-cooling option. Moreover, it was discussed that the setup can be used with different kinds of abuse methods still achieving very defined test temperatures.

Generally, the observed differences in performing an NPT at low temperatures with a conductive or a non-conductive nail once more confirm the difficulties in realizing a reproducible NPT. On one side, the reproducibility can be linked to the TR process itself. On the other side, a reproducible NPT can also be related to the severity of the induced mechanical damage, particularly, at low temperatures. Decreased temperatures can lead to the complete inertization of the cell or at least to mitigated, TR-unlike reactions directly after the abuse test. Moreover, the results show that the conductivity during rethermalization is the key factor for the occurrence of a TR reaction. Relating these results to real systems indicates that the nature, especially, the electrical conductivity of a damaging object has a crucial influence on the TR behaviour during rethermalization of a critically damaged, cooled battery. Nonetheless, disassembling a critical damaged battery at temperatures below its inertization point can greatly enhance the safety of this process.

In summary, the highly precise NPT realized by the herein developed NP tool delivers important insights regarding the definition of minimum requirements for a reproducible NPT supporting future standardizations. Furthermore, the setup allows in-depth investigations of the behaviour of various cell types under abusive conditions at different, precise temperatures supporting the general understanding of TR-mechanisms.

4. Experimental Section

NP Tool: The detailed development of the NP tool is described in Section 2.1 the present section provides an overview of the operation ranges of the tool and the technical description of a NPT. **Table 1** compares the specifications of the two motor setups. The DC (direct current) motor motion accuracy was determined by repeatedly stopping the motor which was triggered with an end switch. During these measurements, the DC motor was operated manually without using a control algorithm. The customized ALI2 linear actuator (MecVel) with a maximum load of 2500 N enabled the integration of an encoder for the DC motor realised by a second shaft end.

NPTs with DC motor were conducted by starting in the upper end position of the tool and performing a movement until either the maximum z-force was reached, or the lower end switch was triggered. For the NPTs with the stepper motor, the nail was moved until it touched the cell surface, which was detected by a rising z-force. Afterwards the NPT was executed with the desired parameters regarding temperature, speed, and penetration depth. In order to ensure the nails' manufacturing accuracies needed, 50 mm hardened steel dart tips with 2.26 mm diameter were used

as nails for all tests presented in this work (Figure 1d). The nail tip has a torpedo-like shape with a length of ≈ 11 mm (see Figure S7, Supporting Information).

The temperature of the LIB-cell was detected by type-K thermocouples which were fixed to the outer cell surface with Kapton tape.

Volumetric Flow Measurement: The volumetric flow can be measured at the test chamber exhaust (shown detailed in Figure 1a). While measuring the exact gas amount emitted from abused LIBs in an open system remains a challenge, the selected system (C310, KIMO) utilizes different sensor types to measure the volumetric flow. The system is calibrated for measuring the volume flow of ambient air. However, the composition of gases emitted from abused LIB-cells is quite different and as well depends on the cell type. To ensure the flow system is measuring in ambient air, the volume/distance between the test chamber and the measurement system is increased. Furthermore, at the beginning of the volume measuring inlet route an additional sensor (CO SCCO 0–500 ppm, KIMO) detects LIB-TR gases by measuring the carbon monoxide concentration. This prevents wrong conclusions of the LIB gas volume in the measurement route due to different gas densities after TR.

The volumetric measurement itself is realized by two sensors which measure in parallel, however, are based on two different detection principles. One sensor works according to the calorimetric principle (hot wire probe SVS 0–30 ms^{-1} , KIMO) and delivers more reliable data for low flow velocities. The other sensor is based on the pressure differential measurement method (flow measuring lance DEBIMO 2–40 ms^{-1} , KIMO). As it is well known that from the TR reaction not only gaseous components emerge, the pressure differential system is also equipped with an automatic air pressure-based cleaning mechanism (EMLR-1, KIMO), which makes this system also robust against particle pollution. The volumetric measurement is also temperature compensated by a type-K thermocouple.

Temperature Control: Precooling Experiments: A cold gas generator (KGW-Isotherm Type: TG-LKF-H 63/50) with a heater power of 630 W and a jet power of 500 W was used to ensure proper tempered conditions for abuse testing. The system ensures a temperature stability of the generated cold gas of ± 0.2 K. The setpoint temperature range is rated from -190 °C to 100 °C. However, the actual temperature reached, and the necessary precooling time of the cell depend on the ambient temperature of the test chamber, the cell size, the cell holder material, the amount of gas leakage from the cell holder to the test chamber, as well as the volumetric flow from the cold gas generator. The detailed overview of the system is explained in Figure 1a.

Temperature Control: Shock Cooling Experiments: For the shock cooling experiments, a home-made tub, withstanding the high occurring TR temperatures, was developed. This tub is based on two welded stainless-steel tubs isolated by Styrofoam. While the inner tub is directly in contact with the liquid nitrogen it is not in direct contact with the outer tub, preventing thermal bridging. The tub can be automatically filled up to its maximum capability of 3 kg liquid nitrogen (measured over the weight change from the Cryotherm Apollo 100 cryo-vessel by an Ohaus Defender 5000 stainless steel dual range scale with 10 g resolution). Due to the isolation of the tub, the evaporation rate of the gaseous nitrogen is below 0.4 L s^{-1} . This is measured by the installed volumetric flow sensor described in Section 2.1. The automatized filling was realised by combining the cryo vessel with a transfer siphon including a magnetic valve (Type: ASCO E262K114S1TD0FL). Afterwards, a home-made elevator lifted up the filled tub. Hereby, a height of 65 mm could be covered, reaching a maximum speed of 5 mm s^{-1} . To ensure a stable temperature before the NPT, two heating elements were included in the cell holder. A cascade control with two PI controllers was developed for the heating elements to set a precise

Table 1. Comparison of 24 V DC motor (transtecno) and stepper motor (AS5918S2804-E, Nanotec).

Motor description	Speed range [mm s^{-1}]	Max. force [N]	Min. step resolution [mm]	Motion Position [mm]	Max penetration depth [mm]
DC motor	10–80	1800	–	± 0.15	40
Stepper motor	0.01–7.00	1200	0.08	± 0.02	40

Table 2. Parameters of the investigated cell types. Details of the NPTs conducted with these cells can be found in Table S1, Supporting Information.

Abbreviation	Type code	Cathode material	Anode materia	Nominal capacity [Ah]	Nominal voltage [V]
NMC-1 to NMC-21	Samsung SDI INR18650-29 E	LiNi _{0.5} Mn _{0.3} Co _{0.2} O ₂	Graphite	2.6	3.7
LFP-1 and LFP-2	LithiumWerks APR18650M1B	LiFePO ₄	Graphite	1.1	3.3

temperature prior NPT. The heating elements are not directly connected to the cell enabling a faster cool down of the cell itself when encountering the liquid nitrogen. Further information about the performance of the system is shown in Figure 6c.

CT-Imaging: X-ray Computed Tomography (XCT) of cells was conducted at BAM (Bundesanstalt für Materialforschung und -prüfung, Berlin, Germany) using two different laboratory micro-CT scanners. Both scanners are equipped with a microfocus X-ray tube (X-ray WorX GmbH). All scans were performed with a tube voltage of 190 kV and at 19 Watt power. Volumes were reconstructed using an in-house written C++ program with an FDK reconstruction algorithm for cone beams geometries.^[37]

FTIR: The measurement of the cell gas composition can optionally be performed by a *Gasmét* FTIR system (Figure 1a). The system consists of a probe with a filter, a heated hose (180 °C), a sampling unit (0.05 L s⁻¹) and the DX4015 FTIR. The gas concentration is measured by an average of 7 s. The FTIR measurement is started before the NPT and runs continuously until the test is finished. The gas concentration from the LIB-cells is typically calculated by a 30 s average 5 min after the TR occurred.

EIS: The NP tool was additionally equipped with a *Gamry* Interface 5000 E potentiostat (Figure 1a), allowing the collection of additional data during the abuse tests.^[38] Electrochemical impedance spectroscopy (EIS) measurements at defined temperature of 20 °C (±2 °C) prior an NPT can ensure for example that the tested cells have similar preconditions. Moreover, the integration of the potentiostat enables further electrochemical investigations of critically damaged cells in the safe environment of the test chamber after an NPT.

Sample Selection and Testing: In this work, all tests were performed with cylindrical 18 650 cells. **Table 2** summarizes the characteristic parameters of the cell types investigated. While the LiFePO₄ cell type is mainly used to validate the quality of the NPT, the LiNi_{0.5}Mn_{0.3}Co_{0.2}O₂ type is used for TR-related tests. An overview of all samples including their respective test parameters can be found in Table S1, Supporting Information.

Supporting Information

Supporting Information is available from the Wiley Online Library or from the author.

Acknowledgements

The authors acknowledge Nawar Yusfi and Oliver Zeh from the Bundesanstalt für Materialforschung und -prüfung for their valuable practical assistance in conducting the abuse tests.

Open Access funding enabled and organized by Projekt DEAL.

Conflict of Interest

The authors declare no conflict of interest.

Data Availability Statement

The data that support the findings of this study are available from the corresponding author upon reasonable request.

Keywords

abuse testing, battery safety, high-precision nail penetration, lithium-ion batteries, thermal runaway

Received: November 1, 2023

Revised: February 1, 2024

Published online:

- [1] W. Huang, X. Feng, X. Han, W. Zhang, F. Jiang, *Cell Rep. Phys. Sci.* **2021**, *2*, 100285.
- [2] S. S. Zhang, K. Xu, T. R. Jow, *J. Power Sources* **2003**, *115*, 137.
- [3] T. R. B. Grandjean, A. A. Jeswinth, A. McGordon, J. Marco in *2020 Fifteenth Int. Conf. on Ecological Vehicles and Renewable Energies (EVER)*, IEEE, Piscataway, NJ **2020**, pp. 1–5.
- [4] T. R. Grandjean, J. Groenewald, J. Marco, *J. Energy Storage* **2019**, *21*, 202.
- [5] X. Liu, D. Ren, H. Hsu, X. Feng, G.-L. Xu, M. Zhuang, H. Gao, L. Lu, X. Han, Z. Chu, J. Li, X. He, K. Amine, M. Ouyang, *Joule* **2018**, *2*, 2047.
- [6] P. Kritzer, H. Döring, B. Emermacher, *ACES* **2014**, *04*, 197.
- [7] Z. Wang, K. Wang, J. Wang, Y. Yang, Y. Zhu, W. Bai, *J. Loss Prev. Process Ind.* **2022**, *79*, 104853.
- [8] Y. Cao, K. Wang, Z. Wang, J. Wang, Y. Yang, X. Xu, *Renewable Energy* **2023**, *206*, 1097.
- [9] W. Mei, L. Zhang, J. Sun, Q. Wang, *Energy Storage Mater.* **2020**, *32*, 91.
- [10] R. V. Bugga, M. C. Smart, *ECS Trans.* **2010**, *25*, 241.
- [11] J. Long, *Detection and characterization of Lithium Plating*, Universitätsverlag der TU, Berlin **2023**
- [12] A. J. Ringsby, K. D. Fong, J. Self, H. K. Bergstrom, B. D. McCloskey, K. A. Persson, *J. Electrochem. Soc.* **2021**, *168*, 80501.
- [13] Y. Li, X. Feng, D. Ren, M. Ouyang, L. Lu, X. Han, *ACS Appl. Mater. Interfaces* **2019**, *11*, 46839.
- [14] L. Aiello, G. Gstrein, S. Erker, B. Kaltenegger, C. Ellersdorfer, W. Sinz, *Batteries* **2022**, *8*, 32.
- [15] A. Abaza, S. Ferrari, H. K. Wong, C. Lyness, A. Moore, J. Weaving, M. Blanco-Martin, R. Dashwood, R. Bhagat, *J. Energy Storage* **2018**, *16*, 211.
- [16] J. Lamb, C. J. Orendorff, *J. Power Sources* **2014**, *247*, 189.
- [17] X. Feng, J. Sun, M. Ouyang, F. Wang, X. He, L. Lu, H. Peng, *J. Power Sources* **2015**, *275*, 261.
- [18] X. Gao, Y. Jia, W. Lu, Q. Wu, X. Huang, J. Xu, *Cell Rep. Phys. Sci.* **2023**, *4*, 101542.
- [19] D. P. Finegan, B. Tjaden, T. M. M. Heenan, R. Jervis, M. Di Michiel, A. Rack, G. Hinds, D. J. L. Brett, P. R. Shearing, *J. Electrochem. Soc.* **2017**, *164*, A3285.
- [20] S. Doose, W. Haselrieder, A. Kwade, *Batteries* **2021**, *7*, 6.
- [21] J. Diekmann, S. Doose, S. Weber, S. Münch, W. Haselrieder, A. Kwade, *J. Electrochem. Soc.* **2020**, *167*, 90504.
- [22] H. Chen, E. Kalamaras, A. Abaza, Y. Tripathy, J. Page, A. Barai, *Appl. Energy* **2023**, *349*, 121610.
- [23] T. Yokoshima, D. Mukoyama, F. Maeda, T. Osaka, K. Takazawa, S. Egusa, S. Naoi, S. Ishikura, K. Yamamoto, *J. Power Sources* **2018**, *393*, 67.

- [24] T. Yokoshima, D. Mukoyama, F. Maeda, T. Osaka, K. Takazawa, S. Egusa, *J. Electrochem. Soc.* **2019**, *166*, A1243.
- [25] S. Huang, X. Du, M. Richter, J. Ford, G. M. Cavalheiro, Z. Du, R. T. White, G. Zhang, *J. Electrochem. Soc.* **2020**, *167*, 90526.
- [26] X. Qi, B. Liu, J. Pang, F. Yun, R. Wang, Y. Cui, C. Wang, K. Doyle-Davis, C. Xing, S. Fang, W. Quan, B. Li, Q. Zhang, S. Wu, S. Liu, J. Wang, X. Sun, *Nano Energy* **2021**, *84*, 105908.
- [27] N. Sunderlin, A. Colclasure, C. Yang, J. Major, K. Fink, A. Saxon, M. Keyser, *J. Energy Storage* **2023**, *63*, 107046.
- [28] K. Nandini, K. Usha, M. S. Srinivasan, M. Pramod, P. Satyanarayana, M. Sankaran, *J. Energy Storage* **2018**, *17*, 409.
- [29] T. R. Grandjean, J. Groenewald, A. McGordon, J. Marco, *J. Energy Storage* **2019**, *24*, 100804.
- [30] R. Leonhardt, N. Boettcher, S. Dayani, H. Markoetter, A. Schmidt, J. Krug v Nidda, *Exploring the Electrochemical and Physical Stability of Lithium-Ion Cells Exposed to Liquid Nitrogen*, **2024**, under review.
- [31] H.-C. A. Shiao, D. Chua, H.-P. Lin, S. Slane, M. Salomon, *J. Power Sources* **2000**, *87*.
- [32] N. Q. Le, J. W. Jeon in *2007 Int. Conf. on Control, Automation and Systems*, IEEE, Seoul, Korea (South) **2007**, pp. 1322–1326.
- [33] S. Dayani, H. Markötter, A. Schmidt, M. Widjaja, G. Bruno, *J. Energy Storage* **2023**, *66*, 107453.
- [34] A. Pfrang, A. Kersys, A. Kriston, D. U. Sauer, C. Rahe, S. Käbitz, E. Figgemeier, *J. Electrochem. Soc.* **2019**, *166*, A3745.
- [35] A. Pfrang, A. Kersys, A. Kriston, R.-G. Scurtu, M. Marinaro, M. Wohlfahrt-Mehrens, *J. Electrochem. Soc.* **2023**, *170*, 30548.
- [36] D. P. Finegan, M. Scheel, J. B. Robinson, B. Tjaden, I. Hunt, T. J. Mason, J. Millichamp, M. Di Michiel, G. J. Offer, G. Hinds, D. J. L. Brett, P. R. Shearing, *Nat. Commun.* **2015**, *6*, 6924.
- [37] L. Feldkamp, L. C. Davis, J. Kress, *J. Opt. Soc. Am* **1984**, *1*, 612.
- [38] M. Spielbauer, P. Berg, M. Ringat, O. Bohlen, A. Jossen, *J. Energy Storage* **2019**, *26*, 101039.